Coherent Nano-scale Ternary Precipitates in Crystallized $Ca_4Mg_{72}Zn_{24}$ Metallic Glass

Y.N. Zhang, X.D. Liu, Z. Altounian, M. Medraj

PII: S1359-6462(12)00811-1
DOI: http://dx.doi.org/10.1016/j.scriptamat.2012.12.028
Reference: SMM 9741

To appear in: *Scripta Materialia*

Received Date: 13 November 2012
Revised Date: 22 December 2012
Accepted Date: 24 December 2012

Please cite this article as: Y.N. Zhang, X.D. Liu, Z. Altounian, M. Medraj, Coherent Nano-scale Ternary Precipitates in Crystallized $Ca_4Mg_{72}Zn_{24}$ Metallic Glass, *Scripta Materialia* (2013), doi: http://dx.doi.org/10.1016/j.scriptamat.2012.12.028

Coherent Nano-scale Ternary Precipitates in Crystallized $Ca_4Mg_{72}Zn_{24}$ Metallic Glass

Y.N. Zhang[1], X.D. Liu[2], Z. Altounian[2] and M. Medraj[1]*
[1] Department of Mechanical Engineering, Concordia University,
1455 de Maisonneuve Blvd. W., Montreal, Quebec, Canada, H3G 1M8
[2] Center for the Physics of Materials and the Department of Physics, McGill University,
3600 University Street, Montreal, Quebec, Canada, H3A 2T8

*Email address: mmedraj@encs.concordia.ca

Abstract

The ternary precipitates in the $Ca_4Mg_{72}Zn_{24}$ metallic glass formed during heat treatment were characterized by differential scanning calorimetry, X-ray diffraction and transmission electron microscopy. The melt-spun sample after heat treatment exhibits nano-scale elongated precipitates of $Ca_2Mg_5Zn_{13}$ distributed at the grain boundaries and plate-like precipitates of $Ca_2Mg_6Zn_3$ in the grain interior of the Mg matrix. Both of these ternary compounds were identified as coherent precipitates with Mg matrix by high resolution TEM images and could result in enhanced mechanical properties.

Keywords: Ca-Mg-Zn system; Magnesium alloys; Metallic glass; Ternary precipitates; TEM.

Mg-based alloys have great potentials for high-performance aerospace and automotive applications owing to their low density, high fuel efficiency, excellent castability and good machinability. However, their limited strength and low corrosion resistance are major shortcomings [1, 2]. Mg-Zn is one of the most promising systems which has moderate strength, corrosion resistance and age hardening response due to the formation

of stable and metastable phases, such as $Mg_{51}Zn_{20}$, MgZn (or $Mg_{12}Zn_{13}$), Mg_2Zn_3 and $MgZn_2$ [3-8]. Addition of Ca up to 0.3 wt.% was reported to increase ductility through grain size refinement [9]. Ca content in Mg alloys improves strength, castability, and creep and corrosion resistance [2]. In addition, Zn and Ca together with Mg form $Ca_2Mg_6Zn_3$ which is more stable than Mg_2Ca binary compound at lower temperatures (<623 K). $Ca_2Mg_6Zn_3$ is responsible for the age hardening behavior and further enhances the strength and creep resistance of Mg-based alloys [10-14]. Recently, Mg-rich Ca-Mg-Zn biocompatible metallic glass having small amounts of Ca (0-8 at.%) has been found suitable for the development of biodegradable implants [15-17]. However, size effects, including grain sizes, can play an important role in age hardening behavior, mechanical properties and biomedical applications [14, 18-20]. To refine the microstructure of Ca-Mg-Zn alloys, we need to study the equilibrium, non-equilibrium phases and their phase relationships.

To date, the Ca-Mg-Zn isothermal section at 608 K was constructed using a combination of the high-throughput diffusion couple technique and equilibrated key alloys [21]. While many researchers have studied the hexagonal $Ca_2Mg_6Zn_3$ compound, the results are contradictory [14, 22-25]. Recently, we reported on the solubility ranges and crystal structures of $Ca_2Mg_6Zn_3$ (IM1, IM denotes intermetallic compound) and another ternary solid solution $Ca_2Mg_5Zn_{13}$ (IM3) at 608 K using scanning electron microscopy (SEM), electron probe micro-analysis (EPMA), transmission electron microscopy (TEM), electron back-scattered diffraction (EBSD) and X-ray diffraction (XRD) results [26, 27]. The $Ca_2Mg_6Zn_3$ (IM1) and $Ca_2Mg_5Zn_{13}$ (IM3) hexagonal ternary compounds were found

to be in equilibrium with the hexagonal close-packed Mg matrix [21] and can contribute to the age hardening response. Recently, we have reported the crystallization characteristics of metallic glasses in the composition range of $Ca_4Mg_{72-x}Zn_{24+x}$ (x=0 to 12, Δx=2) studied through differential scanning calorimetry (DSC), XRD and the temperature dependence of electrical resistance [28]. In this work, to complement these efforts, a combination of rapid solidification and heat treatment was used to achieve a decrease in the grain sizes, formation of stabilized equilibrium phases, refinement of intermetallic particles sizes, and modification of the morphologies of the Ca-Mg-Zn alloy.

Samples with the nominal composition $Ca_4Mg_{72}Zn_{24}$ (at.%) were prepared in an arc-melting furnace with water-cooled copper crucible in an argon atmosphere using a non-consumable tungsten electrode. The starting metals were supplied by Alfa Aesar with purities of 99.98% Mg, 99.99% Zn and 99% Ca. Samples were remelted five times to ensure homogeneity. To compensate for the mass loss of Mg and Zn due to their high vapor pressure, extra 8 and 12 weight percentages of Mg and Zn, respectively, were added to the compositions before melting. The sample was then crushed into appropriate size for single-roller melt-spinning. The melt-spinning was carried out under helium at a pressure of 50 kPa with a wheel tangential speed of 30 m/sec. The resulting ribbons were approximately 2 mm wide and 30 μm thick. The actual composition of the ribbon samples was determined to be $Ca_4Mg_{76}Zn_{20}$ (at.%) using inductively coupled plasma (ICP) and SEM. The difference between these two measurements is ± 0.5 at.% on average.

XRD was firstly used to verify the amorphous state on the free side of each ribbon and to characterize the sample after each exothermic crystallization peak. The XRD patterns were obtained using PANalytical X'pert Pro powder X-ray diffractometer with a CuKα radiation at 45kV and 40mA. The XRD spectrum was acquired from 20 to 120º 2θ with a 0.02º step size with 2 s of a point scan time. The analysis of the X-ray patterns was carried out using X'Pert HighScore Plus Rietveld analysis software in combination with Pearson's crystal database [29]. The thermal stability, glass transition and crystallization temperatures of the as-quenched glassy samples were studied by means of calibrated non-isothermal SETARAM DSC under a continuous flow of purified argon. The samples were placed in a graphite crucible covered with a lid and quickly cooled after the last exothermic peak to room temperature by flowing argon. The heat treated samples were then investigated by XRD and TEM to determine the phases forming after the last crystallization event. Thin specimens for TEM observations were prepared by ion beam milling in a Gatan PIPS Model 691 at 3 to 5 kV from both sides of the ribbon. Philips CM200 TEM operated at 200kV was used to characterize the specimens.

The XRD pattern obtained from the free side of the as-quenched sample is shown on the upper part of Figure 1a. The absence of detectable crystalline diffraction peaks, together with the broad scattering signals around 37º and 67º 2θ, confirmed the amorphous nature of this sample. Figure 1b presents the DSC scan obtained at a constant heating rate of 5 K/min showing the glass transition, four crystallization events (marked by T_{p1}, T_{p2}, T_{p3} and T_{p4}) and melting behavior. The XRD pattern for the sample heated to 583 K is shown in Figure 1a. From a Rietveld full pattern refinement, the crystallographic parameters and

phase amounts of the refined phases for the last crystallization event are presented in Table 1. The atomic coordinates and site occupancy of IM1 and IM3 were taken from our previous findings [26, 27]. After heating beyond the 4th crystallization event (583 K), Mg, IM1 and IM3 phases formed, which is consistent with the Ca-Mg-Zn equilibrium phase diagram [21].

> Figure 1. <

> Table 1. <

The phase type, structure, morphology and coherency with the Mg matrix of the precipitates were characterized by TEM. Figure 2 shows bright field (BF) images of the melt-spun $Ca_4Mg_{72}Zn_{24}$ metallic glass sample, heated beyond the last crystallization event, taken from the $[2\bar{1}\bar{1}0]_{Mg}$ orientation. The images show fine grain of about 200 - 500 nm in size. Compared with grain sizes (1- 2 μm) obtained from the $Ca_{1.0}Mg_{96.7}Zn_{2.3}$ (at.%) alloy through melt spinning reported by Jardim [11], significant improvement in the grain size refinement was achieved in this work.

Elongated precipitates with approximately 500 nm in length were distributed at the grain boundaries of both prismatic and pyramidal planes. Some of those precipitates are located along the grain boundary as shown in Figure 2a and b. Nie and Muddle [30] reported that the multiple precipitates lying on both prismatic and pyramidal planes improve the mechanical strength of Mg alloys. In addition, Oh-ishi et al [14] observed similar elongated precipitates in the $Ca_{0.3}Mg_{98.1}Zn_{1.6}$ (at.%) alloy. According to them, the composition of this alloy is near the two-phase region consisting of α-Mg and $Ca_2Mg_6Zn_3$

(IM1) and the three-phase region consisting of α-Mg, $Ca_2Mg_6Zn_3$ (IM1) and Mg_2Ca in the Ca-Mg-Zn ternary phase diagram. Hence, they have identified these precipitates as Mg_2Ca and/or $Ca_2Mg_6Zn_3$. However, according to our recent research [21], this alloy is located in the three-phase region consisting of α-Mg, $Ca_2Mg_6Zn_3$ (IM1) and $Ca_2Mg_5Zn_{13}$ (IM3) and these precipitates should be $Ca_2Mg_5Zn_{13}$ (IM3) instead of the Mg_2Ca or $Ca_2Mg_6Zn_3$ compounds. The hexagonal structure of IM3 was also indexed and confirmed by means of SAED based on our previous crystallographic study [27]. The selected area electron diffraction (SAED) patterns are shown in Figure 3. Figure 3c and f present the SAED patterns of location A in Figure 3a and location B in Figure 3d, respectively. Two types of crystallographic orientation relationships were found between the IM3 and the hexagonal close-packed Mg matrix. This is for the first time that such a relationship was observed. Figure 3c indicates $[2\bar{1}\bar{1}0]_{Mg}$// $[11\bar{2}3]_{IM3}$ and Figure 3f indicates $[2\bar{1}\bar{1}0]_{Mg}$//$[1\bar{2}10]_{IM3}$. Furthermore, the IM3 ternary precipitate was identified as coherent precipitate with Mg matrix, as shown in high-resolution transmission electron microscopy (HRTEM) images (Figure 4a and b). The mismatch parameter, δ, where $\delta=(d_{IM3}-d_{Mg})/d_{Mg}$ (d value presents lattice spacing) is close to 0, indicating a perfect coherency between the Mg matrix and these IM3 ternary precipitates. Another crystallographic orientation relationship between the IM3 and the Mg matrix was observed in Figure 4b: $[2110]_{Mg}$// $[2110]_{IM3}$, $(0111)_{Mg}$// $(05\bar{5}1)_{IM3}$. The lattice parameters a and c as well as the lattice spacing, d values for IM3, obtained from the SAED patterns (Figure 3, 4a and 4b) show good consistency with the XRD results (Figure 1). Both morphology and coherency of these elongated precipitates $Ca_2Mg_5Zn_{13}$

(IM3) distributed at the grain boundaries of the hcp-Mg matrix are reported for the first time in this work.

In addition to the $Ca_2Mg_5Zn_{13}$ (IM3) elongated precipitates distributed at the grain boundary, fine dispersed plate-like hexagonal $Ca_2Mg_6Zn_3$ (IM1) precipitates were observed in the grain interior, as shown in Figure 2. These $Ca_2Mg_6Zn_3$ (IM1) precipitates varied in size (20-100 nm) and shape (spherical and cuboid plate-like). The hexagonal structure of $Ca_2Mg_6Zn_3$ (IM1) was also indexed and confirmed by means of XRD results and HRTEM image, as shown in Figure 1 and Figure 4c. As illustrated in Figure 4a and c, $Ca_2Mg_6Zn_3$ (IM1) ternary precipitate is also identified as coherent precipitate with Mg matrix due to the very low mismatch δ (less than 2%) through HRTEM image, as shown in Figure 4c. This shows a good consistency with the literature where the stable intermetallic compound $Ca_2Mg_6Zn_3$ has low lattice misfit with the Mg solid solution matrix [12, 14] and proves the experimental accuracy of this work. The orientation relationships between the IM1 and the Mg matrix were observed as: $[2\bar{1}\bar{1}0]_{Mg}//[2\bar{1}\bar{1}0]_{IM1}$, $(01\bar{1}1)_{Mg}//(03\bar{3}2)_{IM1}$, as shown in Figure 4a and c. To summarize, these two types of precipitates forming within the matrix and at the grain boundaries of Mg matrix after the last crystallization event are $Ca_2Mg_6Zn_3$ (IM1) and $Ca_2Mg_5Zn_{13}$ (IM3) ternary compounds confirmed by XRD and TEM results as well as the composition of the sample is consistent with the phase relationship among the Mg, IM1 and IM3 in the Ca-Mg-Zn phase diagram [21].

> Figure 2. <

> Figure 3. <

> Figure 4. <

The ternary precipitates in the $Ca_4Mg_{72}Zn_{24}$ metallic glass formed during heat treatment were characterized by DSC, XRD and TEM. A combination of rapid solidification and heat treatment was used to achieve the refinement of the grains and intermetallic particles sizes, formation of the stable equilibrium ternary phases, modification of the morphologies and verification of the orientation relationship between intermetallic particles and matrix. The heat treated sample after the last crystallization event exhibits two types of precipitates and both of these ternary compounds were identified as equilibrium phases with the Mg matrix. The nano-scale spherical and cuboid plate-like precipitates $Ca_2Mg_6Zn_3$ (IM1) in the grain interior and the elongated precipitates $Ca_2Mg_5Zn_{13}$ (IM3) distributed at the grain boundary are coherent precipitates with the Mg matrix.

Acknowledgments

The authors would like to acknowledge Dr. X.B. Liu of Physics Department of McGill University for useful discussions and suggestions.

References

[1] T.M. Pollock, Science 328 (2010), pp. 986-987.

[2] A.A. Luo, Int. Mater. Rev. 49 (2004), pp. 13-30.

[3] D.Y. Maeng, T.S. Kim, J.H. Lee, S.J. Hong, S.K. Seo, B.S. Chu, Scripta Mater. 43 (2000), pp. 385-389.

[4] J. Buha, Mater. Sci. Technol. A 492 (2008), pp. 11-19.

[5] J. Buha, Mater. Sci. Technol. A 491 (2008), pp. 70-79.

[6] F. Nie, B.C. Muddle, Scripta Mater. 37 (1997), pp. 1475-1481.

[7] T. Zhou, D. Chen, Z.H. Chen, J.H. Chen, J. Alloys Compd. 475 (2009), pp. L1-L4.

[8] M. Aljarrah, M. Medraj, X. Wang, E. Essadiqi, G. Dénès, A. Muntasar, J. Alloys Compd. 438 (2007), pp. 131-141.

[9] O. Beffort, Ch. Hausmann, in: K.U. Kainer (Ed.), Magnesium Alloys and their Applications (2000), pp. 215-220.

[10] P.M. Jardim, G. Solorzano, J.B.V. Sande, Microsc. Microanal. 8 (2002), pp. 487-496.

[11] P.M. Jardim, G. Solorzano, J.B.V. Sande, Mater. Sci. Technol. A 381 (2004), pp. 196-205.

[12] G. Levi, S. Avraham, A. Zilberov, M. Bamberger, Acta Mater. 54 (2006), pp. 523-530.

[13] M. Bamberger, G. Levi, J.B.V. Sande, Metall. Mater. Trans. A 37A (2006), pp. 481-487.

[14] K. Oh-ishi, R. Watanabe, C.L. Mendis, K. Hono, Mater. Sci. Technol. A 526 (2009), pp. 177-184.

[15] B. Zberg, P.J. Uggowitzer, J.F. Löffler, Nat. Mater. 8 (2009), pp. 887-891.

[16] E. Ma, J. Xu, Nat. Mater. 8 (2009), pp. 855-857.

[17] X.N. Gu, Y.F. Zheng, S.P. Zhong, T.F. Xi, J.Q. Wang, W.H. Wang, Biomaterials 31 (2010), pp. 1093-1103.

[18] J.R. Greer, J.T.M.D. Hosson, Prog. Mater. Sci. 56 (2011), pp. 654-724.

[19] D.C. Jang, J.R. Greer, Nat. Mater. 9 (2010), pp. 215-219.

[20] J.-Y. Kim, D. Jang, and J.R. Greer, Adv. Funct. Mater. 21 (2011), pp. 4550-4554.

[21] Y.N. Zhang, D. Kevorkov, F. Bridier, M. Medraj, Sci. Tech. Adv. Mater. 12 (2011), 025003.

[22] R. Paris, Ministère de L'Air 45 (1934), pp. 1-86.

[23] J.B. Clark, Trans. AIME 221 (1961), pp. 644-645.

[24] J.B. Clark, Joint Committee on Powder Diffraction Standards (JCPDS) Card (1961), 12-0266.

[25] T.V. Larinova, W.W. Park, B.S. You, Scripta. Mater. 45 (2001), pp. 7-12.

[26] Y.N. Zhang, D. Kevorkov, J. Li, E. Essadiqi, M. Medraj, Intermetallics 18 (2010), pp. 2402-2411.

[27] Y.N. Zhang, D. Kevorkov, X.D. Liu, F. Bridier, P. Chartrand, M. Medraj, J. Alloys Compd. 523 (2012), pp. 75-82.

[28] Y.N. Zhang, G.J. Rocher, B. Briccoli, D. Kevorkov, X.B. Liu, Z. Altounian, M. Medraj, J. Alloys Compd. (2012), 10.1016/j.jallcom.2012.10.089.

[29] P. Villars, K. Cenzual, Pearson's Crystal Data (2010).

[30] J.F. Nie, B.C. Muddle, Magnesium Alloys and Their Applications (1998), pp. 229-234.

List of Figures Captions

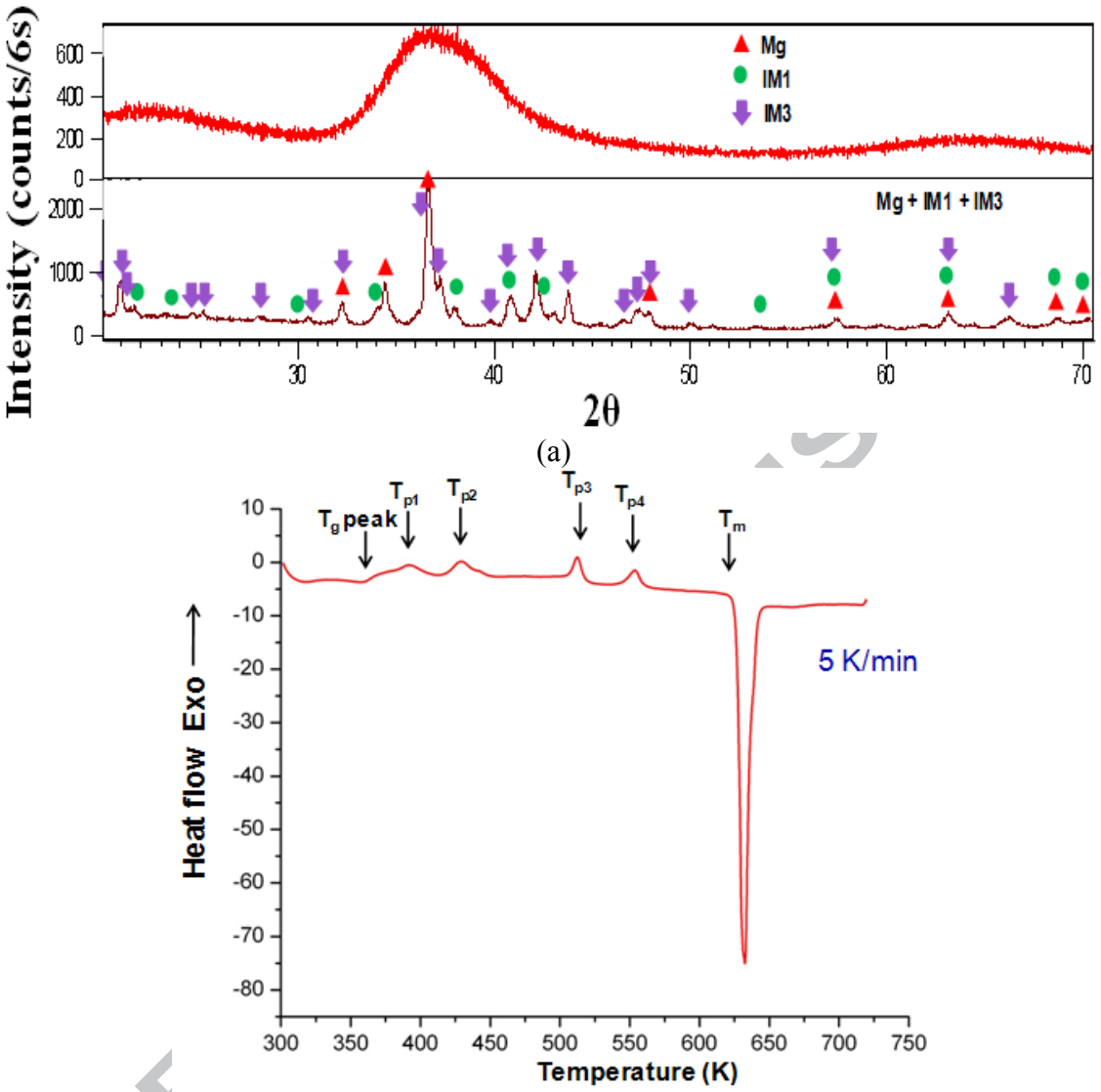

Figure 1. (a) XRD patterns of the $Ca_4Mg_{72}Zn_{24}$ composition obtained from the as-quenched and heated beyond the last crystallization event; (b) DSC curve measured at a constant heating rate of 5 K/min showing the glass transition, crystallization and melting behavior of the $Ca_4Mg_{72}Zn_{24}$ metallic glass.

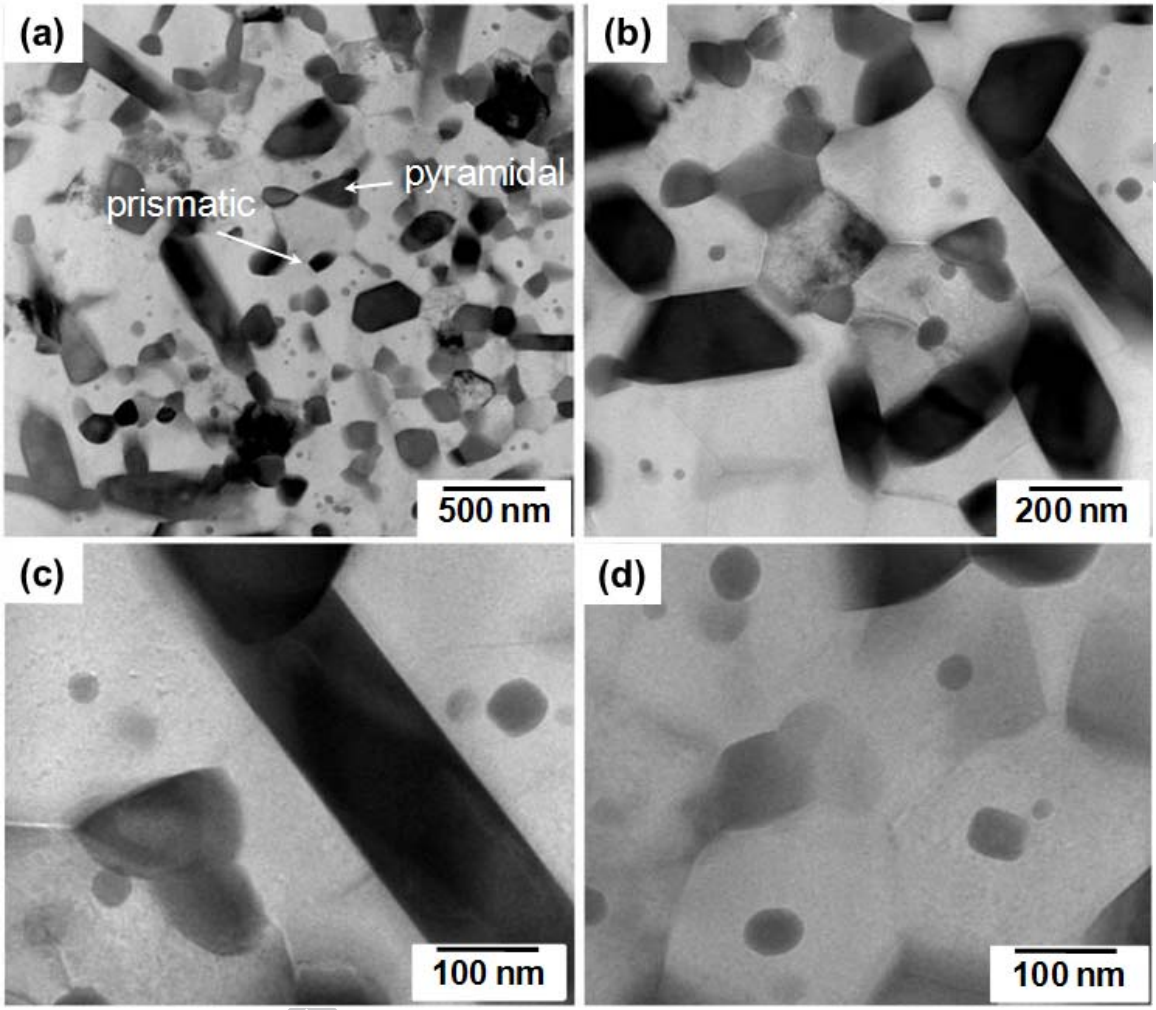

Figure 2. TEM images of the $Ca_4Mg_{72}Zn_{24}$ metallic glass heated beyond the last crystallization event occurring at 583 K taken from the $[2\bar{1}\bar{1}0]_{Mg}$ orientation (a) overview micrograph; (b-d) with increased magnification.

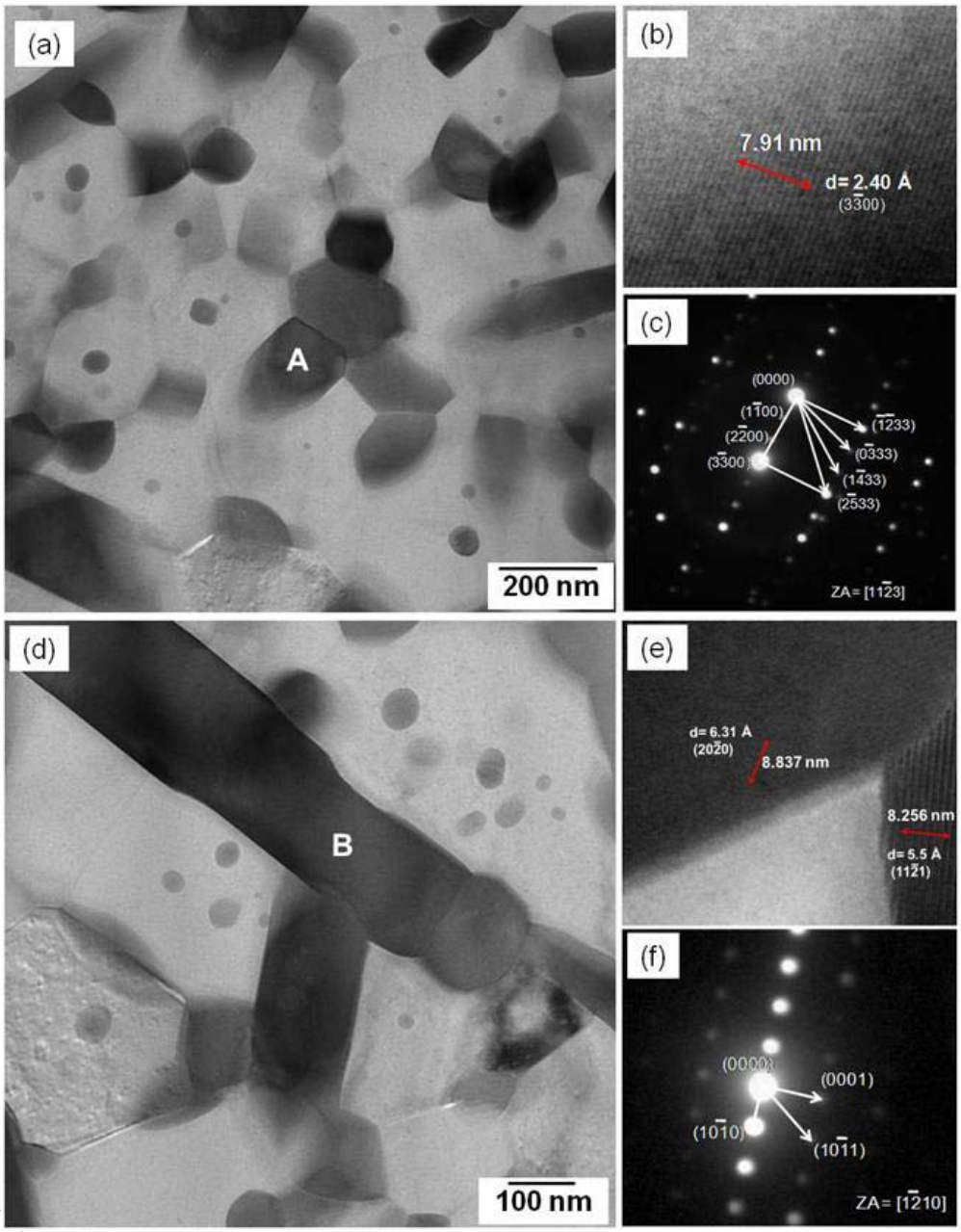

Figure 3. TEM images of the $Ca_4Mg_{72}Zn_{24}$ metallic glass beyond the last crystallization event occurring at 583 K, (a) and (d) taken from the $[2\bar{1}\bar{1}0]_{Mg}$ orientation; (c) and (f) SAED patterns for hexagonal IM3 ternary compound of the $[11\bar{2}3]_{IM3}$ and $[1\bar{2}10]_{IM3}$ orientations, respectively.

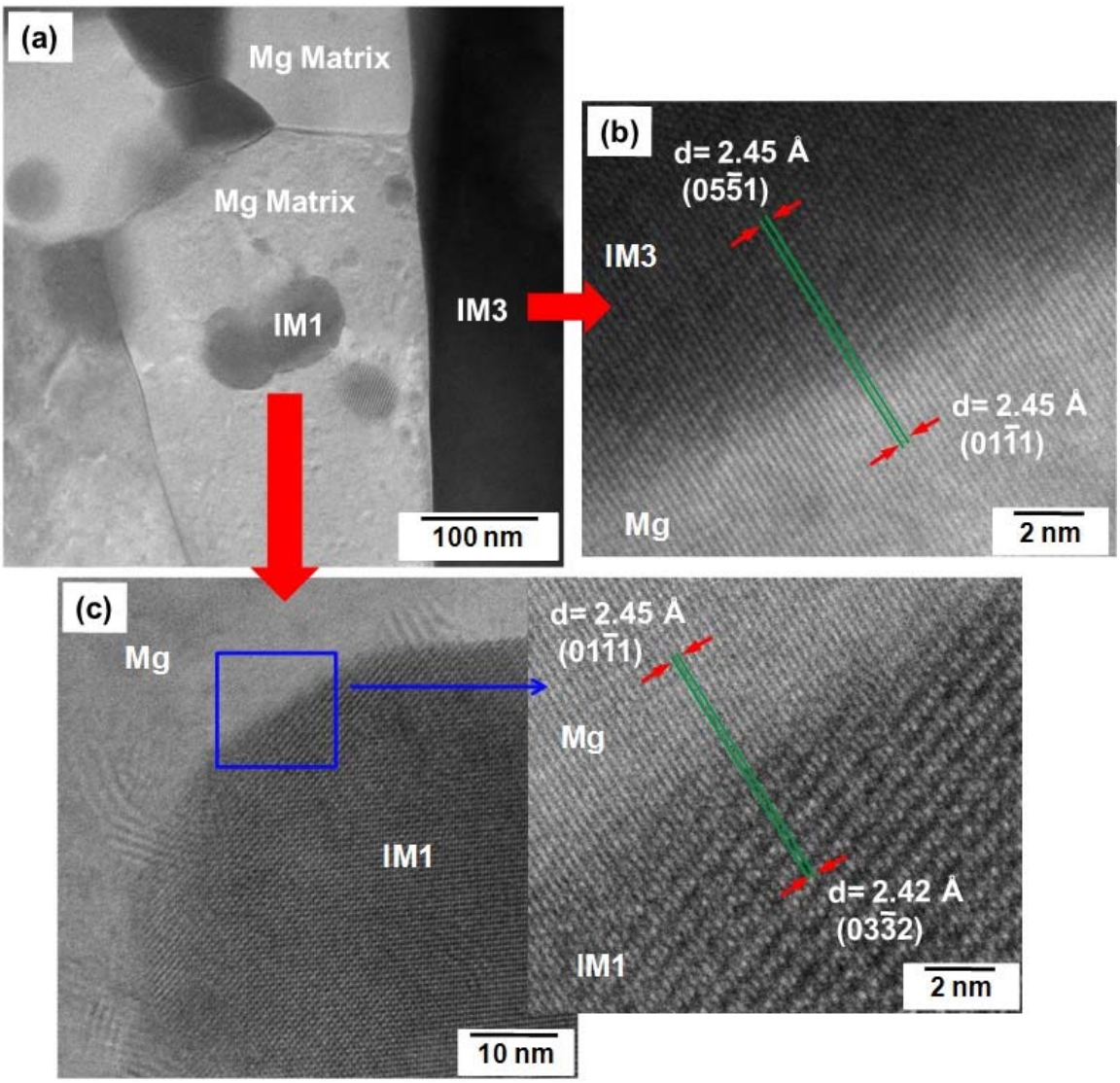

Figure 4. TEM images of the $Ca_4Mg_{72}Zn_{24}$ metallic glass beyond the last crystallization event occurring at 583 K, taken from the $[2\bar{1}\bar{1}0]_{Mg}$ orientation, (a) overview (b) HRTEM image of interface between IM3 and Mg; (c) HRTEM image of interface between IM1 and Mg.

List of Tables Captions

Table 1. The crystallographic parameters and phase amount of the refined phases forming after the last crystallization event of $Ca_4Mg_{72}Zn_{34}$ composition.

Peak number	Phases identified by XRD	Unit cell parameters			Phase amount (wt.%)
		a(Å)	*b*(Å)	*c*(Å)	
P4 (last crystallization event)	Mg	3.206	3.206	5.207	61.6
	$Ca_2Mg_6Zn_3$ (IM1)	9.475	9.475	9.966	8.2
	$Ca_2Mg_5Zn_{13}$ (IM3)	14.742	14.742	8.779	30.2

Graphical Abstract